International Journal of Heat and Fluid Flow 30 (2009) 930–938

Contents lists available at ScienceDirect

International Journal of Heat and Fluid Flow

journal homepage: www.elsevier.com/locate/ijhff

DNS of heat transfer in transitional, accelerated boundary layer flow over a flat plate affected by free-stream fluctuations

Jan G. Wissink [a,*], Wolfgang Rodi [b]

[a] School of Engineering and Design, Howell Building, Brunel University, Uxbridge UB8 3PH, UK
[b] Institute for Hydromechanics, University of Karlsruhe, Kaiserstr. 12, D-76128 Karlsruhe, Germany

ARTICLE INFO

Article history:
Received 14 October 2008
Received in revised form 30 April 2009
Accepted 6 June 2009
Available online 2 July 2009

Keywords:
Heat transfer
Accelerating boundary layer
Streaks

ABSTRACT

Direct numerical simulations (DNS) of flow over and heat transfer from a flat plate affected by free-stream fluctuations were performed. A contoured upper wall was employed to generate a favourable streamwise pressure gradient along a large portion of the flat plate. The free-stream fluctuations originated from a separate LES of isotropic turbulence in a box. In the laminar portions of the accelerating boundary layer flow the formation of streaks was observed to induce an increase in heat transfer by the exchange of hot fluid near the surface of the plate and cold fluid from the free-stream. In the regions where the streamwise pressure gradient was only mildly favourable, intermittent turbulent spots were detected which relaminarised downstream as the streamwise pressure gradient became stronger. The relaminarisation of the turbulent spots was reflected by a slight decrease in the friction coefficient, which converged to its laminar value in the region where the streamwise pressure gradient was strongest.

1. Introduction

Free-stream turbulence in incoming flow can influence strongly heat transfer to turbine blades. The physical mechanisms involved are only just beginning to be understood (Mayle et al., 1998). Mainly two effects of free-stream turbulence impinging on the blade's boundary layer can be distinguished:

(1) Earlier transition on the suction side which leads to an increase in heat transfer due to turbulent motion of the boundary layer flow.
(2) Increase in heat transfer in regions where the boundary layer remains laminar; here one can differentiate between:
   - Pretransitional/inactive regions of the suction side boundary layer.
   - The entire pressure side boundary layer.

Free-stream turbulence can be either uniformly distributed or concentrated in wakes. To be able to predict the effects of free-stream turbulence impinging on a boundary layer one needs to know both the integral length-scale of this turbulence and its turbulence level. When free-stream turbulence is concentrated in wakes, also the frequency of these wakes should be taken into account.

Several experiments have been performed to study the influence of free-stream turbulence on "laminar" heat transfer – that is: the heat transfer in regions where the boundary layer is laminar – and on boundary layer transition. In their experimental studies of laminar heat transfer to a flat plate affected by free-stream fluctuations, Kestin et al. (1961) and Junkhan and Serovy (1967) discovered that in order for these fluctuations to be able to increase heat transfer, the affected laminar boundary layer flow needs to be accelerating. These findings were confirmed by the experiments of Schulz (1986), who measured heat-transfer distributions around a typical fore-loaded airfoil for several free-stream turbulence levels. Along the stagnation region at the leading edge, where the acceleration is very strong, the highest heat transfer was found. On the suction surface, where a laminar to turbulent transition occurs, the main effect was to cause an earlier onset of transition inducing a subsequent increase in heat transfer. Along the pressure side, where the highly accelerated boundary layer remains laminar, the main effect of the free-stream turbulence was to cause a large increase in laminar heat transfer. Liu and Rodi (1994a,b) performed heat-transfer measurements of flow in a model turbine cascade with incoming wakes. With increasing wake-frequency, the heat transfer along both the pressure side – with its strong acceleration – and the favourable pressure gradient portion of the suction side, was found to increase, see also Wissink and Rodi (2006). In the recent experiments of Choi et al. (2004), studying the effect of free-stream turbulence on turbine blade heat transfer, the grid-generated turbulence was shown to affect the heat transfer along both areas of the turbine blade with flow acceleration (i.e. the entire pressure side and approximately the upstream half of the suction side) and also along those areas which exhibit transition to turbulence. Increasing the free-stream turbulence level

* Corresponding author. Tel.: +44 1895 267371.
E-mail address: jan.wissink@brunel.ac.uk (J.G. Wissink).

0142-727X/$ - see front matter © 2009 Elsevier Inc. All rights reserved.
doi:10.1016/j.ijheatfluidflow.2009.06.003

– while keeping the Reynolds number fixed – was shown to lead to an increase in heat transfer.

The aim of the paper is to further elucidate the physical mechanisms that play a role in the interaction of free-stream fluctuations in an accelerating main flow and the boundary layer of a heated object. The present series of DNS concerns the influence of uniformly distributed free-stream turbulence with two prescribed integral length-scales on the laminar heat transfer from a heated flat plate with an accelerating main flow.

2. Computational details

The three-dimensional, incompressible Navier–Stokes equations were discretised using a finite-volume method with a collocated variable arrangement. In space, a second-order accurate central discretisation was used, combined with a three-stage Runge–Kutta method for the time-integration. To avoid the decoupling of the velocity field and the pressure field, the momentum interpolation procedure of Rhie and Chow (1983) was employed. The Poisson equation for the pressure was iteratively solved using the SIP solver of Stone (1968). A more complete description of the computational code can be found in Breuer and Rodi (1996). For the heat transfer, a convection–diffusion equation for the temperature, T, was solved using a second-order accurate central finite-volume method which was again combined with a three-stage Runge–Kutta method for the time-integration. The Prandtl-number was chosen to be $Pr = 0.71$. The code was parallelised using the standard message passing interface (MPI) protocol.

Fig. 1 shows a section at midspan through the computational domain. The shape of the contoured upper wall was chosen such that a uniform area region is obtained immediately downstream of the inflow plane to let the flow settle, followed by a contraction to induce a strong acceleration along a large part of the flat plate. The spanwise size of the computational domain was varied to accommodate free-stream fluctuations with various integral length-scales Λ. The reference length-scale L is implicitly defined in Fig. 1. The flat plate was heated to a fixed temperature of $T = T_0$, while the oncoming outer flow had a temperature of $T = 0.7T_0$. At the surface of the flat plate (i.e. the lower wall) a no-slip boundary condition was prescribed, at the outlet a convective outflow boundary condition was used, and in the spanwise direction periodic boundary conditions were applied. Along the contoured upper wall a free-slip boundary condition was employed. Free-stream fluctuations $(u', v', w')^t$ were generated in a separate LES of isotropic turbulence in a box, see Wissink and Rodi (2006). One single snapshot of the isotropic turbulent velocity field was subsequently selected to introduce fluctuations into the computational domain. Because of the finite number of modes in the snapshot, the spectrum of the introduced fluctuations also had a finite number of modes: It consisted of a base frequency $f_{base} = U_0/D$ (determined by the size of the box D) and a number of discrete frequencies which were all higher harmonics of f_{base}. At the inflow plane, located at $x/L = 0.0$, the free-stream fluctuations $(u', v', w')^t$ were superposed on a Blasius profile with a boundary layer thickness of $\delta_{99} = 0.0040L$ in which the v-velocity component was set to zero, i.e.

$$\begin{pmatrix} u_{in} \\ v_{in} \\ w_{in} \end{pmatrix} = u_b \left\{ \begin{pmatrix} 1 \\ 0 \\ 0 \end{pmatrix} + \frac{1}{U_0} \begin{pmatrix} u' \\ v' \\ w' \end{pmatrix} \right\},$$

where $(u_{in}, v_{in}, w_{in})^t$ is the velocity at the inlet and u_b is the u-component of the Blasius profile. The multiplication by u_b guarantees that the no-slip boundary condition was fulfilled at $y/L = 0$. As shown in Table 1, a total of five simulations were performed at a Reynolds number of $Re = 80000$, based on the free-stream velocity at the inflow plane, U_0, and the length-scale L, implicitly defined in Fig. 1. Simulation T00 was effectively two-dimensional and its purpose was to obtain laminar reference data (i.e. without inflow fluctuations). Simulations T30–T42 were performed using free-stream fluctuations with a level of $Tu = 5\%$ at the inflow plane. The integral length-scale of the free-stream fluctuations at the inflow plane was varied from $\Lambda = 0.0415L$ in Simulations T40–T42 to $\Lambda = 0.0830L$ in Simulation T30. Here Λ is defined as

$$\Lambda = \int_0^{\frac{1}{2}l_z} R_{33}(z')dz',$$

where $R_{33}(z') = cov(w(z_0,t), w(z_0+z',t))/var(w(z_0,t))$ is the two-point correlation function at $x/L = 0$ and arbitrary y location.

Fig. 2 shows every eighth grid-line in a cross-section through the computational domain at midspan. The distribution of grid-points in the mesh was based on experience gained earlier in performing various DNS of flow in low-pressure turbine cascades – see Michelassi et al. (2002) and Wissink (2003) – and produced a reasonable resolution of the flat plate boundary layer. The distance of the wall-nearest grid-point to the flat plate (in wall-units) reaches values between $\Delta_y^+ = 1.2$ and $\Delta_y^+ = 2.2$ in Simulation T40, $\Delta_y^+ = 1.1$ and $\Delta_y^+ = 1.9$ in Simulation T41, and $\Delta_y^+ = 0.6$ and $\Delta_y^+ = 0.95$ in Simulation T42. In the streamwise and spanwise directions, the typical grid size varies from $\Delta_x^+ = 21$, $\Delta z^+ = 10$ to $\Delta_x^+ = 80$, $\Delta z^+ = 39$ in Simulation T40; $\Delta_x^+ = 13.8$, $\Delta z^+ = 5$ to $\Delta_x^+ = 40$, $\Delta z^+ = 15$ in Simulation T41; and $\Delta_x^+ = 9.7$, $\Delta z^+ = 2.6$ to $\Delta_x^+ = 28$, $\Delta z^+ = 7.5$ in Simulation T42. The typical near-wall grid

Table 1
Overview of the simulations performed. Λ is the integral length-scale of the free-stream fluctuations at the inflow plane and l_z is the spanwise size. The level of the free-stream fluctuations added at the inflow plane in Simulations T30–T42 was $Tu = 5\%$ and the Reynolds number – based on inflow velocity and the length-scale L (see Fig. 1) – was $Re = 80000$.

Simulation	Grid	l_z	Λ
T00	$902 \times 294 \times 4$	$0.0003L$	–
T30	$902 \times 294 \times 512$	$1.4L$	$0.0830L$
T40	$902 \times 294 \times 256$	$0.7L$	$0.0415L$
T41	$1366 \times 366 \times 512$	$0.7L$	$0.0415L$
T42	$1980 \times 450 \times 1024$	$0.7L$	$0.0415L$

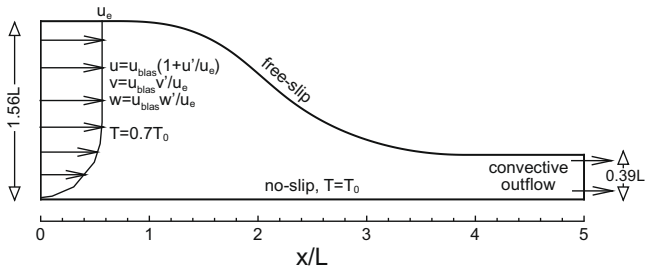

Fig. 1. Spanwise cross-section through the computational domain of Simulations T00, T30, T40.

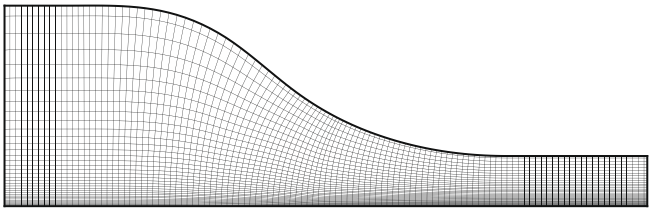

Fig. 2. Mesh at midspan showing every eighth grid-line.

sizes given above indicate that the boundary layer is well resolved in Simulation T42 and reasonably well in Simulations T40 and T41.

3. Results

3.1. Grid-refinement study

Simulations T40–T42 are part of a grid-refinement study, which was performed to further assess the quality of the meshes.

Figs. 3 and 4 show the results of this study. In Fig. 3 a comparison is given of the mean friction coefficient, C_f (left pane) and the shape factor, H (right pane). In the region upstream of $x/L = 3.4$, there is virtually no influence of refining the grid on C_f and H. The small differences observed are most likely related to the occurence of turbulent spots (that can be seen in Figs. 9–11), which in one simulation may be slightly more intense or occur slightly more often than in the other. The increase in the friction coefficient in Simulation T40 that is observed downstream of $x/L \approx 3.2$ – where the favourable pressure gradient weakens – is a result of transition to turbulence: as some of the streaks become unstable, turbulent spots are formed that grow as they are convected downstream where they eventually amalgamate to form a fully turbulent boundary layer.

As can be seen in the right pane, upstream of $x/L \approx 1.3$, the shape factor gradually declines from the laminar value of $H = 2.6$ at $x/L = 0$ to the mildly turbulent value of $H \approx 2$ at $x/L = 1.3$. Downstream of the plateau between $x/L = 1.3$ and $x/L = 1.4$, the shape factor gradually rises again indicating a relaminarisation of the flow. Laminar values of H are again obtained around $x/L = 3$. Even though the integral length-scales of the free-stream fluctuations are identical, it is only in Simulation T40 that both the shape factor and C_f indicate that the boundary layer flow undergoes transition to turbulence immediately upstream of $x/L = 4$. This is directly related to the resolution of the boundary layer, which in Simulation T40 is somewhat too coarse to describe accurately the dynamics of the small-scale fluctuations.

In order to study the effect of grid-refinement on the heat transfer, in Fig. 4 (left pane) the Nusselt numbers Nu obtained in the simulations T40, T41 and T42 are compared to one another. Nu is used as a measure for the heat transfer from the flat plate to the outer flow and is defined by $Nu = \frac{hL}{k}$, where k is the thermal diffusivity and h is the heat transfer coefficient at the wall defined by

$$h = \frac{q_w}{T_0 - \alpha T_0} = \frac{-k\frac{\partial T}{\partial y}}{T_0 - \alpha T_0} = \frac{-k}{(1-\alpha)L}\frac{\partial\left(\frac{T}{T_0}\right)}{\partial\left(\frac{y}{L}\right)},$$

where the unit of h is W/(m^2 K). In this relation, q_w is the heat flux at the wall and $\alpha = 0.7$ is the ratio between the temperatures of the outer flow and the blade. In the laminar (also referred to as pretransitional) region of the boundary layer – upstream of $x/L = 3.4$ – the Nusselt numbers obtained in the Simulations T40–T42 are virtually the same. A sudden increase in Nu, caused by the boundary layer flow undergoing transition between $x/L = 3.4$ and $x/L = 4.0$ (also evidenced by the values of C_f and H in Fig. 3), is only observed in Simulation T40 which has the coarsest grid.

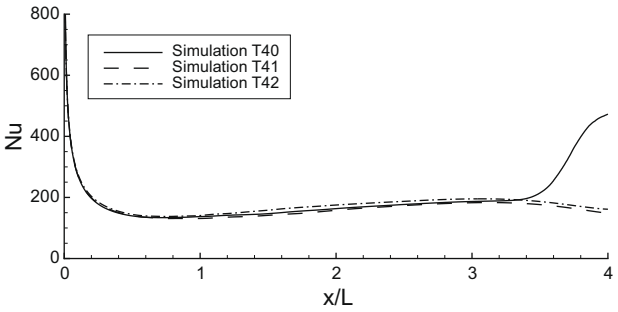

Fig. 4. Nusselt number Nu along the flat plate for Simulations $T40$–$T42$ listed in Table 1.

In the further analysis of the flow the focus will be on the best resolved simulation, T42, and on the Simulations T00 and T30. Though the latter two simulations have a similar resolution as Simulation T40, this is judged to be sufficient since in the region of interest, upstream of $x/L = 3.4$, the resolution of Simulation T40 is found to be adequate. Further, because the integral length-scale of the free-stream fluctuations is larger in Simulation T30 than in Simulation T40, in the former the free-stream fluctuations are better resolved on the same grid. That this is sufficient in Simulation T30 is further supported by the fact that the boundary layer does not undergo transition upstream of $x/L = 4$. The reason for this is that the streak instability is triggered by relatively small-scale free-stream fluctuations which in Simulation T30 are not as strong as in Simulation T40. Because the integral length-scale is larger, less energy is contained in the smaller scales.

3.2. Time-averaged quantities

Fig. 5 (left) displays the wall static-pressure distribution $C_p = \frac{\bar{p}-\bar{p}_{ref}}{\frac{1}{2}U_{ref}^2}$ along the flat plate from Simulation T00. The C_p-distribution shown is characteristic for all simulations. The reference values for the mean pressure $\bar{p}_{ref}$ and the mean velocity U_{ref} were extracted at $x/L = 0.2$, $y/L = 1.4$. Around $x/L = 0.5$ the pressure gradient is observed to be virtually zero. Between $x/L \approx 1$ and $x/L \approx 4$ the pressure gradient is strongly favourable and downstream of $x/L = 4$ it again becomes zero. In the strongly favourable pressure gradient (FPG) region, the boundary layer flow is stabilised and transition is suppressed. Fig. 5 (right) shows the acceleration parameter $K = \left(\frac{U_0 L}{Re u^2}\right)\frac{\partial u}{\partial x}$ extracted in the middle of the computational domain from Simulation T00. Between $x/L = 0$ and $x/L \approx 3.9$ the acceleration parameter is found to be larger than zero. In the region $1.4 < x/L < 3.0$, the acceleration parameter K is

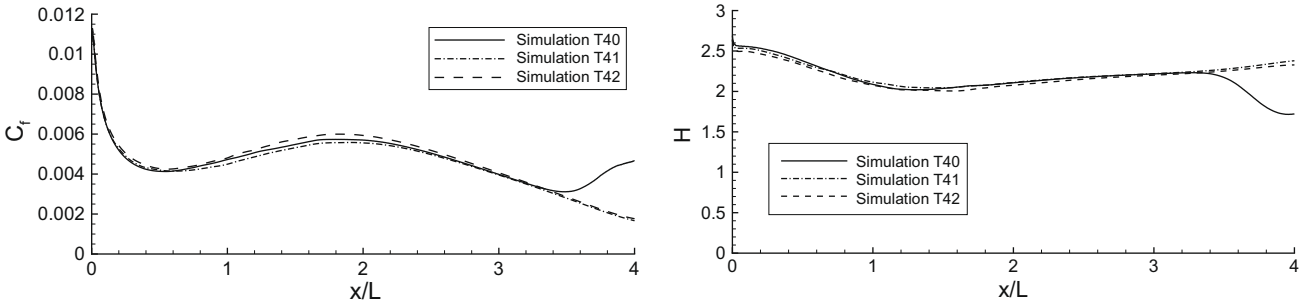

Fig. 3. Mean friction coefficient C_f (left) and shape factor H (right) along the flat plate for Simulations $T40$–$T42$ listed in Table 1.

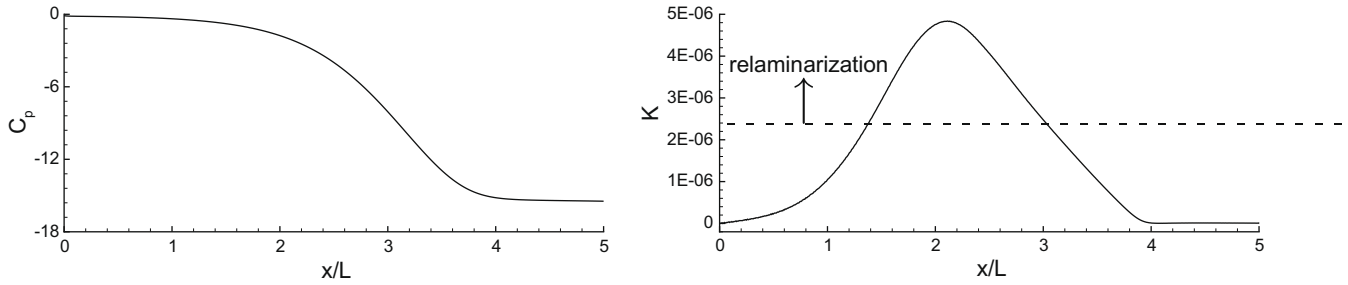

Fig. 5. Simulation T00, left: wall static-pressure coefficient C_p along the flat plate; right: acceleration parameter K in the middle of the computational domain.

larger than 2.5×10^{-6}, which – according to the criterion of Jones and Launder (1973) – is sufficiently strong for a turbulent boundary layer flow to relaminarise. The strongest acceleration ($K \approx 4.8 \times 10^{-6}$) is found at $x/L \approx 2.1$. Compared to the values of K obtained in the stagnation region of an aerodynamic body, the values obtained here are only moderate. For instance, in the simulation of flow around a circular cylinder at $Re_D = 3300$ (based on free-stream velocity and cylinder diameter, see also Wissink and Rodi (2008)), in the immediate vicinity of the stagnation line, K assumes values that are several orders of magnitude larger than the maximum value obtained in the present simulation. Moreover, if in the cylinder case the stagnation line is identified by $\phi = 0^\circ$ – where ϕ is the angle associated with the circumferential coordinate – in the entire sector $-81^\circ < \phi < 81^\circ$ the acceleration parameter K is found to be larger than 2.5×10^{-6}. For the flow along the suction side of the turbine blade investigated in Wissink and Rodi (2006), K is larger than 2.5×10^{-6} in the entire region upstream of $x/L = 0.4$.

Fig. 6 (upper pane) shows the boundary layer thickness, δ_{99}, along the flat plate obtained in the Simulation T00. In the FPG region, at $x/L \approx 3.2$, δ_{99} reaches a (local) minimum value of $0.00723L$ – a factor 5.7 times smaller than the integral length-scale Λ of the free-stream fluctuations in Simulations T40–T42 and a factor 11.5 smaller than the value of Λ obtained in Simulation T30. The latter value of the integral length-scale comes very close to the optimum integral length-scale $\Lambda_{opt} \approx 10\delta_{99}$ of the free-stream turbulence that was advocated by Dullenkopf and Mayle (1995) as being most effective in causing an increase in laminar heat

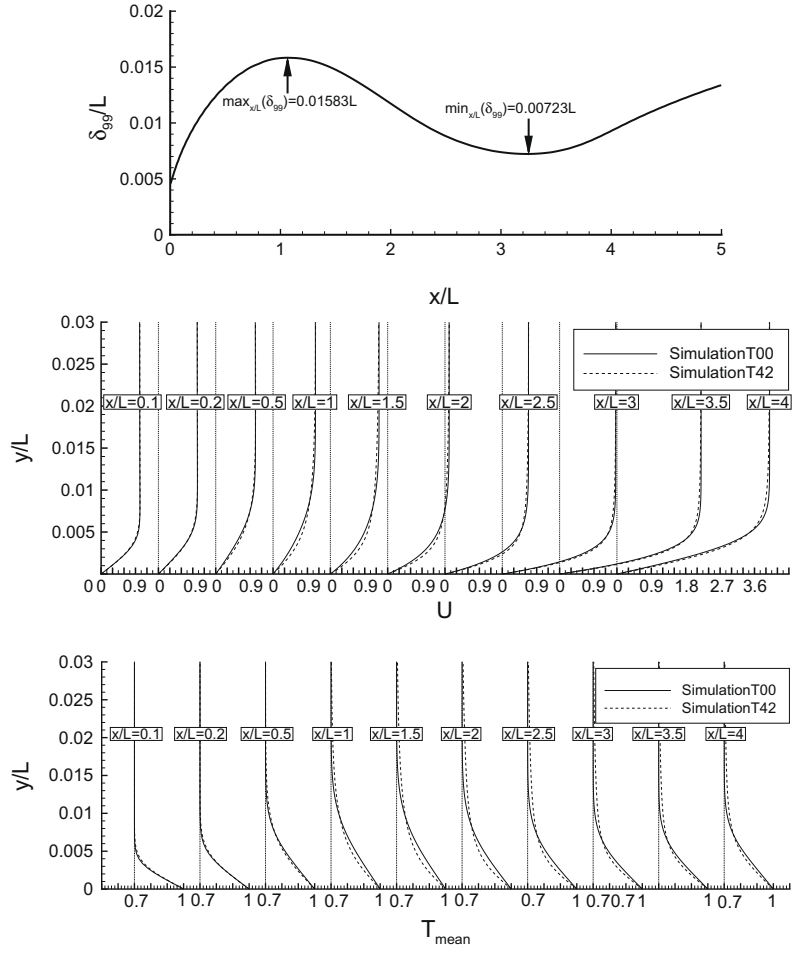

Fig. 6. Upper pane: boundary layer thickness δ_{99} in Simulation T00. Middle pane: comparison of boundary layer profiles from Simulations T00 and T42. Lower pane: comparison of thermal boundary layer profiles from Simulations T00 and T42.

transfer. The maximum value of $\delta_{99} = 0.01583L$, reached at $x/L \approx 1.0$, is about 2.6 times smaller than Λ in Simulations T40–T42 and about 5.2 times smaller than Λ in Simulation T30. The middle pane of Fig. 6 shows a comparison of the actual boundary layer (mean U-velocity) profiles at $x/L = 0.1, 0.2, 0.5, 1.0, 1.5, \ldots, 4.0$ obtained in Simulations T00 and T42. The boundary layer profiles from both simulations are very similar apart from some slight deviations at $x/L = 1, 1.5, 2$, where in Simulation T42 fluctuations have disturbed the boundary layer. These fluctuations are damped and disappear farther downstream because of the accelerating outer flow. The fluctuations, through $\overline{u'v'}$ (see Fig. 7), diffuse the boundary layer in Simulation T42 in the outer region, leading to a slower approach of the velocity to the free-stream velocity. The resulting nominal increase in the thickness of the layer is, as a consequence, not well defined and hence not directly included in Fig. 6 (upper pane). Because of similar effects, also the temperature profiles from Simulation T42 (displayed in the lower pane) exhibit a rather slow approach to the free-stream value. Away from the wall, compared to the velocity profiles, the effect of free-stream fluctuations on the temperature profiles is found to be more significant and extends farther out as the heat flux $\overline{v'T'}$ goes to zero only at $y/L \approx 0.06$ (see Fig. 8). Closer to the wall, the temperature profiles of Simulations T00 and T42 can be seen to be rather similar apart from the slightly fuller profiles obtained for $x/L \geqslant 1$ in Simulation T42 that is caused by the free-stream fluctuations.

Fig. 7 (upper left pane) shows the mean friction coefficient, C_f, along the flat plate for Simulations T00, T30 and T42, see Table 1. Compared to the fully laminar Simulation T00, between $x/L \approx 0.3$ and $x/L \approx 2.8$ the C_f levels in Simulations T30 and T42 are somewhat elevated with a maximum increase at $x/L \approx 1.5$ of 13% in Simulation T30 and approximately 25% in Simulation T42. The increase in C_f is explained by the occurence of turbulent spots (that can be seen in Figs. 9–11). The differences observed between Simulations T30 and T42 are most likely related to a more frequent/intense appearance of turbulent spots in Simulation T42. Owing to the stronger favourable pressure gradient in the downstream region, these turbulent spots relaminarise as they are convected downstream. For $x/L > 1.5$ the C_f-level slowly returns to its laminar value in both Simulations T30 and T42. Because the friction coefficient assumes laminar values in the vicinity of $x/L = 3$, we can conclude that in this region any increase in Nu is a true example of an increase in laminar heat transfer which is solely caused by the presence of streaks.

Fig. 7 (upper right pane) shows the time-averaged shape factor, H, along the flat plate for Simulations T00, T30 and T42. Compared to the laminar Simulation T00, the shape factors in Simulations T30

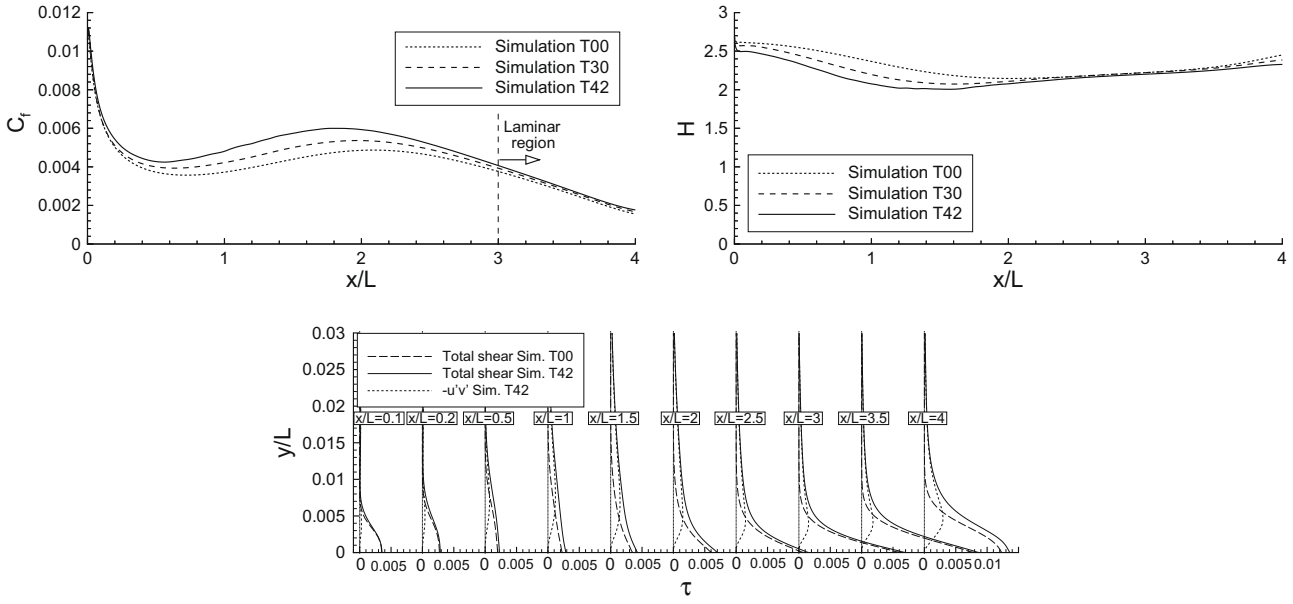

Fig. 7. Upper part: comparison of Simulations T00 (laminar), T30 ($\Lambda = 0.0830L$) and T42 ($\Lambda = 0.0415L$), left: friction coefficient and right: shape factor. Lower part: total and fluctuation-induced shear stress from Simulation T42 and total (viscous) shear stress from Simulation T00.

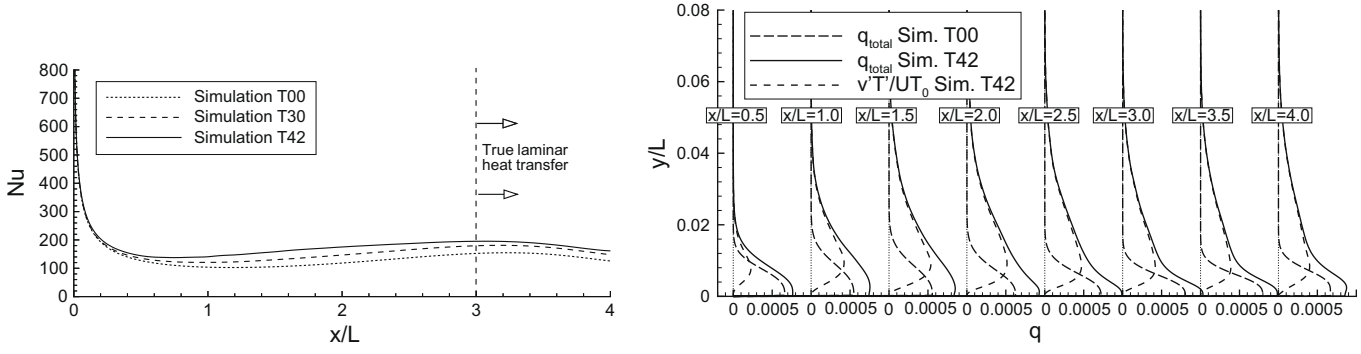

Fig. 8. Left: Nusselt number along the flat plate; comparison of Simulations T00 (laminar), T30 ($\Lambda = 0.0830L$) and T42 ($\Lambda = 0.0415L$). Right: wall-normal total and fluctuation-induced heat flux at several locations in the flat plate boundary layer from Simulation T42 and total heat flux from Simulation T00.

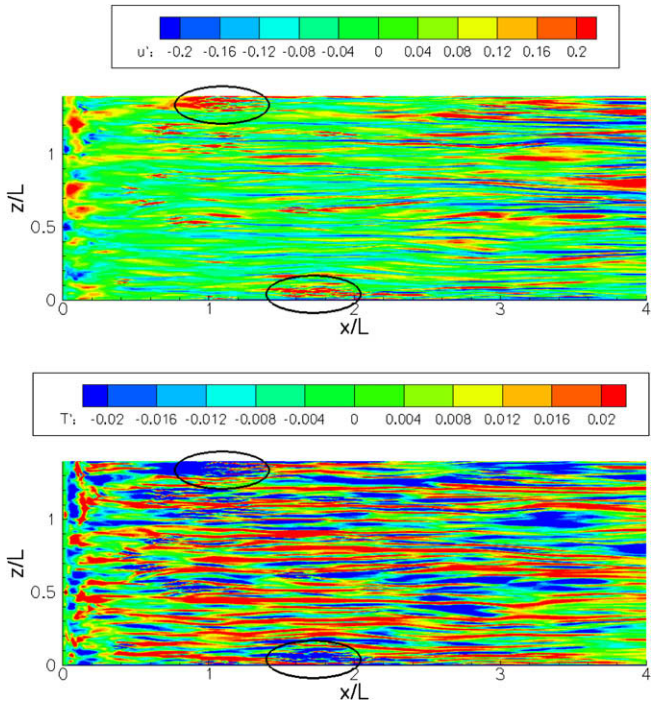

Fig. 9. Simulation T30: grid plane close to the flat plate with contours of the streamwise velocity fluctuations (upper pane) and temperature fluctuations ($T' = T - \bar{T}$) (lower pane). The dark ellipses identify turbulent(-like) spots.

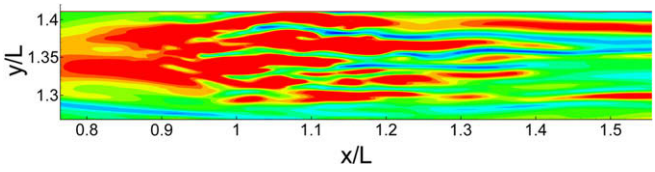

Fig. 10. Simulation T30: zoomed view of the upper turbulent spot in the upper pane of Fig. 9. The scaling of u' can be found in Fig. 9.

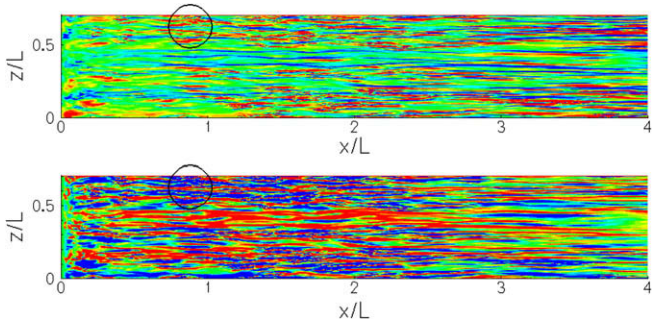

Fig. 11. Simulation T42: grid plane close to the flat plate with contours of the streamwise velocity fluctuations u' (upper pane) and temperature fluctuations ($T' = T - \bar{T}$) (lower pane). The dark ellipses identify turbulent(-like) spots. The scaling of u' and T' can be found in Fig. 9.

and T42 are decreased upstream of $x/L = 2.5$, which evidences the fact that the boundary layer flow is to some extent transitional. The largest decrease can be seen in Simulation T42, which indicates that transition in Simulation T42 reaches a more advanced stage, with more frequent and/or stronger turbulent spots than in Simulation T30. In both Simulations T30 and T42, a gradual growth in H towards the laminar values of Simulation T00 can be observed in the region $1.1 < x/L < 2.5$. Downstream of $x/L = 2.5$, the shape factors in all simulations virtually coincide with one another, indicating that the flow is virtually laminar in all simulations. Compared to the shape factor, however, the friction coefficient appears to be more sensitive with respect to the presence of small pockets of turbulence in the flow as it indicates the boundary layer to turn fully laminar somewhat farther downstream (see above).

Fig. 7 (lower pane) shows the total shear stress

$$\tau = \frac{1}{Re}\frac{\partial\left(\frac{U}{U_0}\right)}{\partial\left(\frac{y}{L}\right)} - \frac{\overline{u'v'}}{U_0^2}$$

of Simulations T00 and T42 and the shear stress due to fluctuations, $-\frac{\overline{u'v'}}{U_0^2}$, of Simulation T42 at several locations $x/L = 0, 1, 0.2, 0.5, 1.0, \ldots, 4.0$ along the flat plate. Because of the absence of free-stream fluctuations in Simulation T00, $\overline{u'v'} = 0$ and the total shear stress is identical to the viscous stress $\frac{1}{Re}\frac{\partial\left(\frac{U}{U_0}\right)}{\partial\left(\frac{y}{L}\right)}$. In Simulation T42, the fluctuations cause the shear stress to extent further away from the wall (up to $y/L \approx 0.03$) leading to the slower approach of the free-stream velocity mentioned already. In the lower part of the boundary layer, approaching the wall, the viscous stress clearly dominates, but the presence of turbulent spots increases the total stress τ at some locations leading to an increase in C_f.

In Fig. 8 (left pane), the Nusselt number obtained in Simulations T30 and T42 is compared to its laminar distribution as obtained in Simulation T00. In the region between $x/L = 1$ and $x/L = 3.4$, in Simulation T42 an increase in Nu in the range 20–40% can be observed, depending on the location along the plate. Upstream of $x/L = 3$, the Nusselt number obtained in Simulation T42 can be seen to be somewhat larger than the one obtained in Simulation T30. This is a direct consequence of the difference in integral length-scale which is reflected by differences in the spectral distribution of energy among the various scales of the free-stream turbulence. From the figure we can conclude that the energy contained in those free-stream modes that are most effective in the triggering of boundary layer disturbances responsible for the increase in Nu is higher in Simulation T42 than in Simulation T30, even though the integral length-scale Λ in Simulation T42 is smaller than Λ in Simulation T30, which is closer to the value of Dullenkopf and Mayle (1995) advocated for maximum Nu increase.

Fig. 8 (right pane) shows the total wall-normal heat flux

$$q_{total} = \frac{\overline{v'T'}}{U_0 T_0} - \frac{1}{Pr\,Re}\frac{\overline{\partial\left(\frac{T}{T_0}\right)}}{\partial\left(\frac{y}{L}\right)}$$

from Simulations T00 and T42 and the wall-normal heat flux due to fluctuations, $\frac{\overline{v'T'}}{U_0 T_0}$ from Simulation T42 ($\frac{\overline{v'T'}}{U_0 T_0} = 0$ in Simulation T00) in the flat plate boundary layer at $x/L = 0.5, 1.0, \ldots, 4.0$. In Simulation T42, the unsteady motion in the free-stream induces fluctuations in the boundary layer that result in a non-zero wall-normal heat flux not only in its upper part, but also above the boundary layer up to about $y/L \approx 0.06$. In the lower part of the boundary layer, the presence of the wall significantly damps the wall-normal fluctuations. Because of this, also the fluctuation-induced normal heat flux becomes negligible. Those fluctuations that do reach the lower part of the boundary layer induce low-speed streaks (see Figs. 9 and 11 below) that form due to a lift-up mechanism, similar to the one that generates low-speed streaks in a turbulent boundary layer. It can be seen that in the region where the laminar boundary layer initially develops ($x/L = 0.5$) the importance of the upward transport of heat due to fluctuations is relatively small; the importance gradually increases downstream until $x/L = 1.5$ – where the acceleration parameter assumes values larger than $K = 2.5 \times 10^{-6}$. Further downstream, the maximum fluctuation-induced heat flux slowly begins to decrease and finally becomes approximately constant beyond $x/L = 3$. Compared to Simulation T00, the effect of the

free-stream fluctuations on the total heat flux in the lower part of the boundary layer of Simulation T42 is far more significant than the effect that the fluctuations have on the total shear stress (see also Fig. 7).

When the acceleration parameter decreases, the boundary layer does not immediately turn turbulent. This is explained by the gradual decrease of the rms values of the streamwise velocity, u_{rms}, in the free-stream from $u_{rms} = 0.05U_0$ at $x/L = 0$ to $u_{rms} < 0.02U_0$ for $x/L \geqslant 3.0$.

3.3. Instantaneous quantities

Figs. 9 and 11 show a grid plane close to the surface of the flat plate with contours of the streamwise velocity fluctuations u' in the upper panes and contours of the temperature fluctuations in the lower panes for the Simulations T30 and T42, respectively. The location of the grid plane is such that y/L varies from 0.0028 near $x/L = 0$ to 0.0014 near $x/L = 4$ or – in terms of wall-units – $10 < y^+ < 20$.

All snapshots in the upper panes clearly show the presence of low-speed and high-speed streaks in the FPG region of the flat plate. The low-speed streaks form as low-speed (hot) fluid originating from the bottom of the boundary layer moves upwards, while the high-speed streaks form as high-speed fluid from the top of the boundary layer moves downwards. The black elipses identify turbulent-like spots that are observed in all simulations. These spots are formed in a region upstream of $x/L = 2$ where the favourable pressure gradient is still relatively mild. As can be seen from the acceleration parameter K shown in Fig. 5 (right), the acceleration of the outer flow reaches a peak at $x/L \approx 2.2$. Because of this strong acceleration ($K > 2.5 \times 10^{-6}$), the turbulent-like spots relaminarise as they are convected downstream. This supports the relaminarization criterion used by Jones and Launder (1973), see also Fig. 5 (right pane). A zoomed view of the upper turbulent spot in Fig. 9 is shown in Fig. 10, where the streamwise structures can be seen to become increasingly finer in the downstream direction.

The lower panes of Figs. 9 and 11 show contours of the temperature fluctuations T', in a snapshot of the temperature field from Simulations T30 and T42, respectively. By comparing T' to u' – displayed in the upper panes – a correlation can be seen between areas of high temperature and the presence of low-speed streaks. High-speed streaks, on the other hand, are observed to correspond to areas of relatively low temperature.

Fig. 12 shows the instantaneous temperature T/T_0 and the streamwise velocity fluctuations $-u'/U_0$ from Simulation T42 along the spanwise line at $x/L = 1$ in the plane shown in Fig. 11. The variations in T/T_0 are closely mirrored by the variations in $-u'/U_0$, which confirms the observation made above of a correlation of areas of high temperature and the occurence of low-speed streaks. Similarly, a correlation between areas of low temperature and the presence of high-speed streaks can also be seen.

Fig. 13 shows a comparison between Simulations T30 and T42 of the fluctuating streamwise velocity u'/U_0 in a cross-section through the boundary layer at $x/L = 1$. It can be seen that the distance between the streaks in Simulation T30 is somewhat larger than in Simulation T42. This is likely to be a direct consequence of the larger integral length-scale of the free-stream fluctuations introduced at the inflow plane of Simulation T30. As evidenced in Fig. 8, compared to Simulation T30, at $x/L = 1$ the higher-wavenumber streamwise-fluctuations introduced into the boundary layer in Simulation T42 lead to a larger increase in Nu. However, the observed fluctuations partly reflect the presence of turbulent spots, which appear to be more frequent in Simulation T42 than in Simulation T30 and are mainly responsible for the difference in Nusselt numbers observed in the two simulations.

Fig. 14 shows a series of six cross-sections at $x/L = 0.5, 1.5, 2.0 2.5, 3.0, 3.5$ with fluctuating velocity vectors in the (y,z)-directions from Simulation T42 combined with contours of the instantaneous temperature field T/T_0. The boundary layer thickness according to Fig. 6 is included and also the thickness of the thermal boundary layer, δ_T, which is defined here as the height where the mean temperature from Simulation T42 has reduced from T_0 at the flat plate to approximately $0.715T_0$. The scaling of the vectors is identified by reference vectors located at the upper left of each pane. As the streamwise flow accelerates, vortical structures in the free-stream get stretched and, as a result, their axes increasingly align with the direction of flow. As a consequence of the stretching, the structures become thinner and the streamwise component of the vorticity vector increases in strength. The latter is reflected in the figure by an increasingly intense rotation in the free-stream that can be observed when moving in the downstream direction from $x/L = 1.5$ to $x/L = 3.0$. Especially at $x/L = 2.5$ and $x/L = 3.0$ a very intense rotation is present in the vicinity of the flat plate. Compared to the viscous boundary layer, the thickness of the thermal boundary layer (which has a compariable size at $x/L = 0.5$) can be seen to grow significantly in the downstream direction owing to the fluctuation-induced normal heat flux.

To obtain a more detailed impression, in Fig. 15 the y-coordinate of the cross-sections at $x/L = 2.5$ and $x/L = 3.0$ has been stretched and the density of the vector field has been increased. In the cross-section at $x/L = 2.5$, near $z/L = 0.11$, a strong vortex can be seen to impinge on the boundary layer, sweeping hot fluid from the surface of the plate upwards. Similar events can be seen

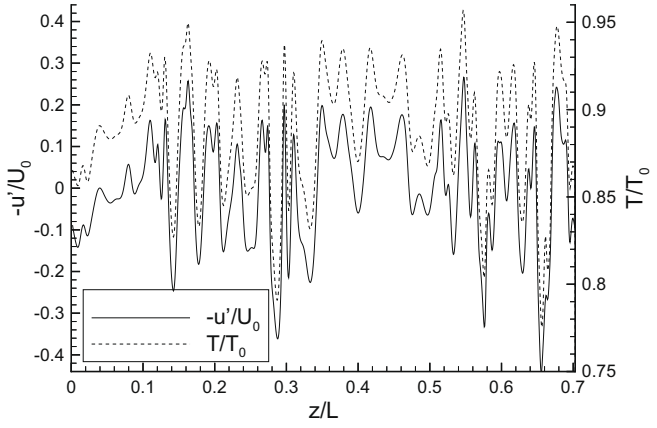

Fig. 12. Simulation T42: cross-section at $x/L = 1$ through the plane shown in Fig. 11 showing $-u'/U_0$ and T/T_0.

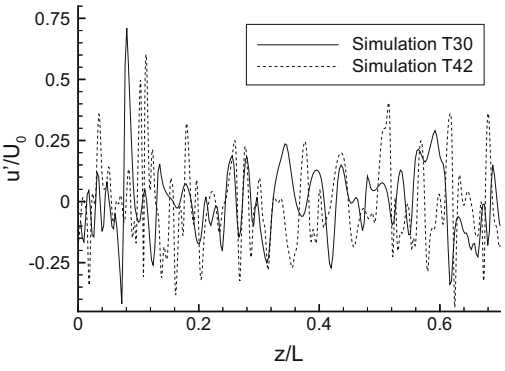

Fig. 13. Simulations T30 and T42: cross-sections at $x/L = 1$ through the planes shown in Figs. 9 and 11 showing u'/U_0.

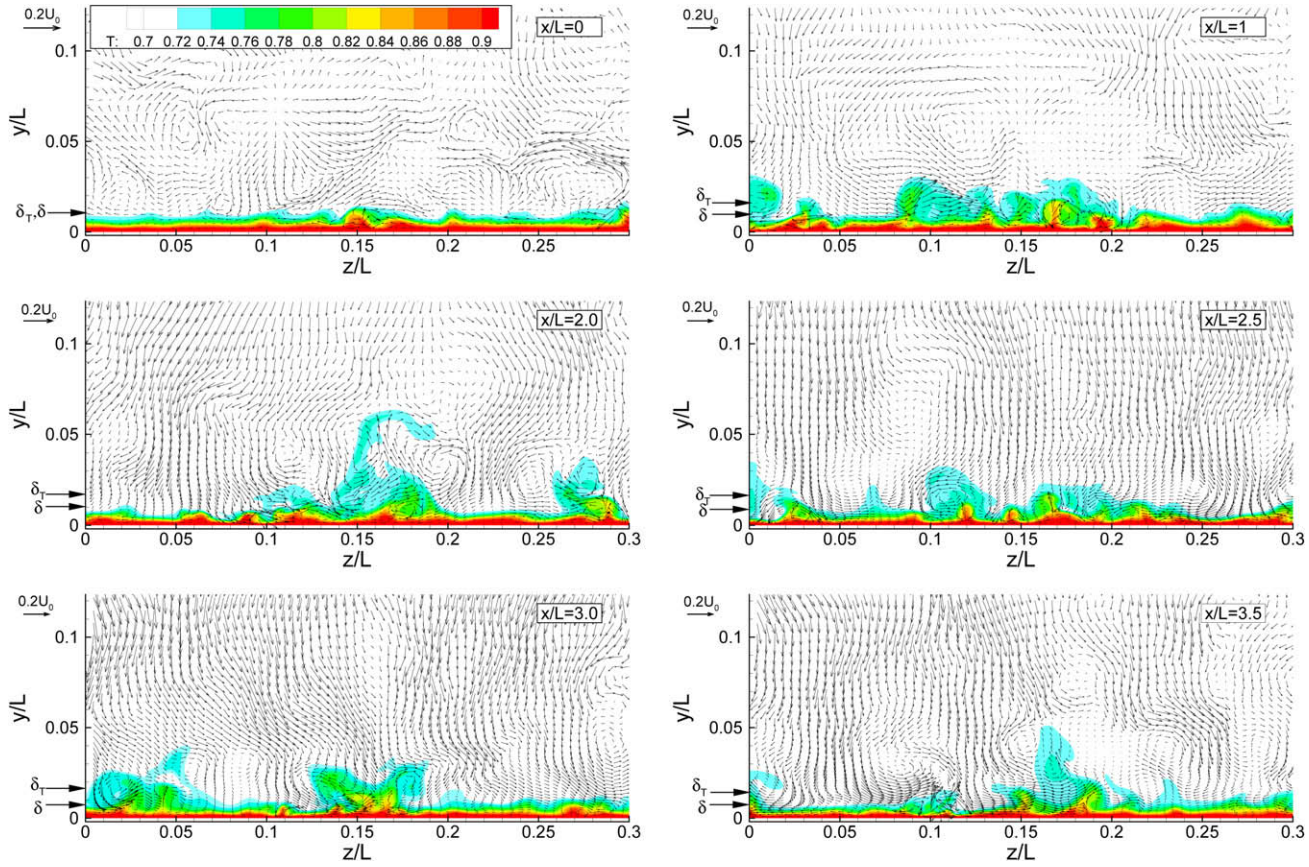

Fig. 14. Simulation T42: vector field of the fluctuating velocity in the cross-sections $x/L = 0.5, 1.5, 2.0, 2.5, 3.0, 3.5$ along the flat plate, showing every seventh vector in the y and z directions. The contours correspond to the instantaneous temperature T, δ_T identifies the approximate thickness of the thermal boundary layer and δ identifies the thickness of the viscous boundary layer.

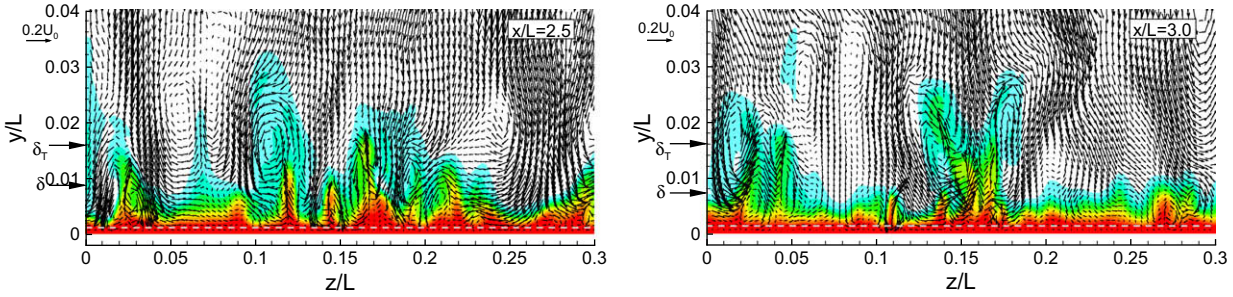

Fig. 15. Simulation T42: Stretched view of the vector field of the fluctuating velocity in the cross-sections $x/L = 2.5, 3.0$ along the flat plate, showing every fifth vector in the y and z directions. The contours correspond to the instantaneous temperature T, the thickness of the boundary layer is identified by δ, the thickness of the thermal boundary layer is identified by δ_T and the horizontal dotted lines identify the location of the plane shown in Fig. 11.

all along this cross-section of the plate. Also at $x/L = 3.0$, impinging rotating structures can be seen to sweep hot (low speed) fluid upwards while cool (low speed) fluid is transported towards the flat plate. This interchange of low speed and high-speed fluid is reflected by the appearance of low- and high-speed streaks as observed in Figs. 9 and 11. The diameter of the rotating structures is about 4—5 times the boundary layer thickness δ, which approximately corresponds to the integral length-scale Λ employed in this simulation (see Table 1 and Fig. 6, upper pane).

4. Conclusions

Three-dimensional Direct Numerical Simulations of flow over and heat transfer from a heated flat plate with and without free-stream fluctuations have been performed at a Reynolds number of $Re = 80\,000$. The special shape of the upper wall of the computational domain induced a strong favourable pressure gradient along a significant portion of the flat plate. The free-stream fluctuations ($Tu = 5\%$ at the inflow plane) were generated in a separate large-eddy simulation of isotropic turbulence in a box. By rescaling the size of the box, the integral length-scale of the free-stream fluctuations was varied.

In all simulations, the presence of free-stream fluctuations is found to trigger low-speed and high-speed streaks in the boundary layer flow. The effect of the acceleration is twofold. Firstly, it stretches the free-stream vortical structures causing them to become more intense and to align with the direction of flow. Secondly, it stabilises the boundary layer flow, which not only

prevents streak instability but also promotes the relaminarisation of young turbulent spots.

As the strong streamwise vortices impinge on the boundary layer, cool outer (high speed) fluid is transported towards the flat plate while hot (low speed) fluid is swept away from the flat plate towards the free-stream. This mechanism promotes heat transfer and causes the appearance of low-speed and high-speed streaks inside the boundary layer. The location of the low-speed streaks identifies the location of hot fluid and the location of high-speed streaks identifies the location of relatively cold fluid. The small turbulent spots that were observed upstream of $x/L = 2.0$ increase heat transfer by inducing an intense local mixing of hot and cold fluid.

In all simulations with free-stream fluctuations, the occurence of turbulent spots along the upstream half of the plate was found to lead to an elevated level of the friction coefficient, compared to the laminar situation. As the turbulent spots relaminarise, the friction coefficient was found to reduce to its laminar level. The location of relaminarisation was found to coincide with the acceleration parameter K assuming values in excess of $K = 2.5 \times 10^{-6}$. The effect of changing the integral length-scale of the free-stream turbulence on the Nusselt number increase in the laminar part of the boundary layer flow was found to be very small for the two Λ values considered. As a secondary effect it was observed that the number of turbulent spots increases when the energy contained in the small scales of the free-stream fluctuations increases.

Acknowledgements

The authors would like to thank the Steering Committee of the Supercomputing Facilities in Bavaria (HLRB) for granting computing time on the Altix high performance computing cluster, and the Steering Committee of the Scientific Supercomputer Centre (SSC) in Karlsruhe for granting access to the HP-XC1 supercomputer.

References

Breuer, M., Rodi, W., 1996. Large eddy simulation for complex flow of practical interest. Flow Simulation with High-Performance Computers II, Notes on Num. Fluid Mech, vol. 52. Vieweg Verlag, Braunschweig.

Choi, J., Teng, S., Ladeinde, F., 2004. Effect of free-stream turbulence on turbine blade heat transfer and pressure coefficients in low Reynolds number flows. Int. J. Heat Mass Trans. 47, 3441–3452.

Dullenkopf, K., Mayle, R.E., 1995. An account of free-stream-turbulence length scale on laminar heat transfer. ASME J. Turbomach. 117, 401–406.

Jones, W.P., Launder, B.E., 1973. The calculation of low-Reynolds number phenomena with a two-equation model of turbulence. Int. J. Heat Mass Trans. 16, 1119–1130.

Junkhan, G.H., Serovy, G.K., 1967. Effects of free-stream turbulence and pressure-gradient on flat plate boundary layer velocity profiles and on heat transfer. ASME J. Heat Trans. 89, 169–176.

Kestin, J., Maeder, P.F., Wang, H.E., 1961. Influence of turbulence on heat transfer from plates with and without a pressure gradient. Int. J. Heat Mass Trans. 3, 133–154.

Liu, X., Rodi, W., 1994a. Velocity measurements in wake-induced unsteady flow in a linear turbine cascade. Exp. Fluids 17, 45–58.

Liu, X., Rodi, W., 1994b. Surface pressure and heat transfer measurements in a turbine cascade with unsteady oncoming wakes. Exp. Fluids 17, 171–178.

Mayle, R.E., Dullenkopf, K., Schulz, A., 1998. The turbulence that matters. ASME J. Turbomach. 120, 402–409.

Michelassi, V., Wissink, J.G., Rodi, W., 2002. Analysis of DNS and LES of flow in a low-pressure turbine cascade with incoming wakes and comparison with experiments. Flow Turbul. Combust. 69, 295–329.

Rhie, C.M., Chow, W.L., 1983. Numerical study of the turbulent flow past an airfoil with trailing edge separation. AIAA J. 21, 1525–1532.

Stone, H.L., 1968. Iterative solution of implicit approximations of multidimensional partial differential equations. SIAM J. Numer. Anal. 5, 530–558.

Schulz, A., 1986. Zum einfluß höher Einstromturbulenz, intensiver Kühlung und einer Nachlaufströmung auf den außeren Wärmeübergang einer konvektiv gekühlten Gasturbinenschaufel. PhD. Thesis, U. Karlsruhe, Karlsruhe, Germany.

Wissink, J.G., 2003. DNS of separating, low-Reynolds number flow in a turbine cascade with incoming wakes. Int. J. Heat Fluid Flow 24, 626–635.

Wissink, J.G., Rodi, W., 2006. Direct numerical simulation of flow and heat transfer in a turbine cascade with incoming wakes. J. Fluid Mech. 569, 209–247.

Wissink, J.G., Rodi, W., 2008. Numerical study of the near wake of a circular cylinder. Int. J. Heat Fluid Flow 29, 1060–1070.